MoS$_2$-MoO$_{3-x}$ hybrid cocatalyst for effectively enhanced H$_2$ production photoactivity of AgIn$_5$S$_8$ nano-octahedrons

Shuaishuai Song[1], Jinming Wang[1], Tianyou Peng[*], Wenli Fu, Ling Zan

College of Chemistry and Molecular Sciences, Wuhan University, Wuhan 430072, PR China

ARTICLE INFO

ABSTRACT

A new binary Mo-based cocatalyst consisting of partially reduced α-MoO$_3$ (MoO$_{3-x}$) nanoparticles and few-layer MoS$_2$ nanosheets is deposited on AgIn$_5$S$_8$ nano-octahedrons (Octa-AIS) with only (111) facets exposed *via* an *in situ* growth process, in which the oxygen-deficient MoO$_{3-x}$ nanoparticles enable facile charge transport due to its high conductivity, while the few-layer MoS$_2$ nanosheets provide more active sites and then excellent catalytic property for H$_2$ evolution. The resultant MoS$_2$-MoO$_{3-x}$ hybrid cocatalyst utilizes the best properties of each component while mitigating their deficiencies, and thus realizes an effective enhancement of visible-light-driven H$_2$ evolution activity on Octa-AIS as compared with the single co-catalyst (such as MoS$_2$, MoO$_{3-x}$, and even Pt nanoparticles). This study not only presents a rare example of binary Mo-based cocatalyst consisting of MoS$_2$ and MoO$_{3-x}$ components, but also paves a new way to develop an inexpensive photocatalytic system for energy conversion to achieve highly efficient H$_2$ evolution without noble metal-loading.

1. Introduction

Since the first report on the photoelectrochemical splitting water into H$_2$ and O$_2$ with TiO$_2$ electrode in 1972 [1], photocatalytic H$_2$ evolution over semiconducting materials is considered as one of the promising solutions to the growing energy crisis due to its potential application in clean hydrogen production from water. Generally, expanding the spectral absorption range is one of the strategic subjects in the field of photocatalysis since most of the transition metal oxide semiconductors used have no suitable bandgap energy and/or structures to eff ;ectively utilize the visible light of sunlight. Whereas the total solar energy (AM1.5G) mainly contains ∼53% visible light (400 nm < λ < 800 nm), ∼43% infrared rays (λ > 800 nm) and ∼4% ultraviolet rays (λ < 400 nm) [2–8]. To circumvent the problem of those metal oxide semiconductors, ternary chalcogenides (I-III-VI, I = Cu, Ag; III = Al, In, Ga; VI = S, Se, Te) with adjustable spectral absorption range have been extensively studied in the field of photocatalysis [9–16]. Among which, AgIn$_5$S$_8$ with a suitable bandgap energy (∼1.68 eV) and the maximum absorption wavelength at ∼700 nm can be used for visible-light-responsive photocatalytic application. Therefore, various methods such as co-precipitation, chemical bath, and hydrothermal methods have been developed to synthesize AgIn$_5$S$_8$ or its composites [10–16]. For instance, a hydrothermal process was recently adopted to synthesize AgIn$_5$S$_8$ nano-octahedrons with exposed

{111} facets and single-crystalline feature in our group [16].

As we know, cocatalyst is recognized as critical factor in determining the photocatalytic performance since it can promote the interfacial charge transfer, reduce the activation energy of the catalytic reaction, and even improve the stability of photocatalysts [2–4,17–20]. Up till now, precious metal Pt with large work function is the commonly used co-catalyst to capture the photogenerated electrons and promote the proton reduction reaction [2,3,19]. Nevertheless, the scarcity and high cost of Pt do not allow the large-scale application as cocatalyst for H$_2$ evolution [18], and thus developing efficient, stable, and earth-abundant cocatalyst remains a very challenging task in the field of photocatalysis [17–20]. Among which, nanostructured molybdenum disulfide (MoS$_2$), a layered crystal structure consisting of S-Mo-S "sandwiches" held together by van der Waals force [21–25], has been widely studied as cocatalyst for photocatalysis [4,26–29]. For example, Zong et al. [4] reported that MoS$_2$ on CdS synthesized by heat treatment of (NH$_4$)$_2$MoS$_4$ in H$_2$S flow acquired better H$_2$ evolution activity than Pt. Similarly, the H$_2$ evolution performance of mesoporous graphitic carbon nitride (mpg-CN) under visible light can be significantly improved by gas-controlled growing thin layers of MoS$_2$ on mpg-CN surface [27]. Nevertheless, the above syntheses of MoS$_2$ nanostructures usually employed thermal treatments of H$_2$S, which is toxic and harmful to human beings due to its highly reactive nature [4,22–27]. Also, solution phase synthesis was developed to fabricate

---

MoS$_2$/graphene hybrid co-catalyst on TiO$_2$ nanoparticles with a synergetic eff;ect between MoS$_2$ and graphene components, which serve as an electron collector and a source of active adsorption sites [28], respectively.

It was reported that the active edge sites of MoS$_2$ are the under-coordinated S-atoms of MoS$_2$ [26], but more studies are needed on the catalytic activity for H$_2$ evolution since multi-layer MoS$_2$ as co-catalyst is limited by the relatively low active sites and inferior conductivity along certain crystallographic directions [26,30]. For example, nanocrystallization of MoS$_2$ have been developed to expose more edge sites for enhancing the H$_2$ evolution activity. On the other hand, orthorhombic α-MoO$_3$ with a layered structure stacked by bilayer MoO$_6$ octahedra sheets through van der Waals forces is widely employed in heterogeneous catalysis, capacitors, and lithium-ion battery applications [30–33]. Although intrinsic α-MoO$_3$ material has seldom been reported as a catalyst for H$_2$ evolution reaction since it has no active edges [33], the partially reduced α-MoO$_3$ (MoO$_{3-x}$) nanocatalyst with mixed Mo^{5+}/Mo^{6+} oxidation states and oxygen-deficient structure is beneficial for the electrochemical H$_2$ evolution reactions [30]. In order to circumvent the limitations of MoS$_2$, core-shell nanowires with MoO$_{3-x}$ cores (~20–50 nm) and conformal MoS$_2$ shells (~2–5 nm) produced by low-temperature sulfidization was synthesized, and it was found that the oxygen-deficient MoO$_{3-x}$ retains the layered orthorhombic α-MoO$_3$ structure which enable facile charge transport due to its high conductivity, and the conformal MoS$_2$ shell can provide more active sites and excellent catalytic activity [34]. Nevertheless, very little attention has been focused on the studies of Mo-based hybrid co-catalyst consisting of MoO$_{3-x}$ and MoS$_2$ for photocatalytic H$_2$ evolution application.

Since the partially reduced MoO$_{3-x}$ has high conductivity, and the MoS$_2$ nanocrystals can provide excellent catalytic activity [33,34], here we try to elucidate and discuss the co-catalyst performance of a new binary Mo-based hybrid cocatalyst (MoS$_2$-MoO$_{3-x}$) on AgIn$_5$S$_8$ nano-octahedrons (Octa-AIS) with high crystallinity and few defects in the exposed {111} facets, which was derived from a hydrothermal process according to our previous report [16]. The Mo-based hybrid co-catalyst consisting of partially reduced α-MoO$_3$ (MoO$_{3-x}$) nanoparticles and few-layer MoS$_2$ nanosheets was deposited on the Octa-AIS surface through a one-step solid-state reaction (SSR) process of ammonium molybdate ((NH$_4$)$_6$Mo$_7$O$_{24}$) and thiourea (SC(NH$_2$)$_2$) at 380 °C for 3 h under N$_2$ atmosphere. The resultant binary Mo-based cocatalyst can effectively improve the visible-light-responsive H$_2$ evolution activity of the Octa-AIS, and thus demonstrating a new route toward earth-abundant cocatalysts for highly efficient H$_2$ evolution system without noble metal-loading.

2. Experimental

2.1. Material preparation

AgIn$_5$S$_8$ nano-octahedrons (Octa-AIS) were synthesized through a hydrothermal process according to our previous report [16]. Typically, a mixture of AgNO$_3$ (0.2 mmol) and In(NO$_3$)$_3$·4.5H$_2$O (1.0 mmol) was dissolved in DI water (60 mL) under magnetically stirring, and then thioacetamide (H$_2$CSNH$_2$) (5.0 mmol) was added under vigorously stirring for 15 min. After adjusting the pH value to 10.6 by using NaOH solution (1.0 M), the mixed solution was transferred into a Teflon-lined stainless-steel autoclave (80 mL) for heat treating at 180 °C for 20 h. After cooling naturally, the precipitate was centrifuged, washed with DI water and ethanol several times, and then dried in a vacuum oven at 80 °C overnight.

MoS$_2$-MoO$_{3-x}$ loaded Octa-AIS was prepared through a one-pot solid-state reaction (SSR) process. Typically, the as-prepared Octa-AIS (0.10 g) was ground with DI water (1.0 mL) containing different amounts of ammonium molybdate ((NH$_4$)$_6$Mo$_7$O$_{24}$·4H$_2$O) and thiourea (SC(NH$_2$)$_2$) for 30 min and then heated at 380 °C for 3 h under N$_2$ atmosphere. By varying the addition amounts of (NH$_4$)$_6$Mo$_7$O$_{24}$·4H$_2$O

and SC(NH$_2$)$_2$ whilst keeping the same Mo:S molar ratio (1:1), 1%, 3%, 5% and 7% (weight percentage) Mo-based cocatalyst-loaded Octa-AIS (denoted as MoS$_2$-MoO$_{3-x}$/Octa-AIS) were produced.

Also, two contrast samples (MoO$_{3-x}$/Octa-AIS and MoS$_2$/Octa-AIS) with 3% (weight percentage) MoO$_{3-x}$ or MoS$_2$ were prepared through a similar process. MoO$_{3-x}$/Octa-AIS was derived from the pyrolysis of (NH$_4$)$_6$Mo$_7$O$_{24}$ in the presence of Octa-AIS, while MoS$_2$/Octa-AIS prepared through the one-pot SSR process of (NH$_4$)$_6$Mo$_7$O$_{24}$/SC(NH$_2$)$_2$ with Mo:S molar ratio of 1:20. Moreover, Pt as co-catalyst was deposited on the Octa-AIS surface through a photoreduction reaction process. Typically, Octa-AIS (0.20 g) and a certain amount of H$_2$PtCl$_6$ solution (0.077 M) were dispersed in methanol aqueous solution (50 mL, 10 vol% methanol) with an ultrasonic bath for 30 min and then irradiated by a 500 W high pressure Hg-lamp for 3 h under magnetically stirring, then Pt/Octa-AIS was obtained by centrifugation and washed with DI water several times, and dried in a vacuum oven at 80 °C overnight.

For comparison, 3% MoS$_2$-loaded AgIn$_5$S$_8$ (MoS$_2$/AIS) was synthesized *via* a one-pot hydrothermal process similar to our previous report [16]. Typically, a mixture of AgNO$_3$ (0.2 mmol), In(NO$_3$)$_3$·4.5H$_2$O (1.0 mmol) and (NH$_4$)$_6$Mo$_7$O$_{24}$·4H$_2$O (0.035 mmol) were dissolved in DI water (60 mL) under magnetically stirring, and then SC(NH$_2$)$_2$ (5.0 mmol) was added under vigorously stirring for 15 min. After adjusting the pH value to 10.6 by using NaOH solution (1.0 M), the mixed solution was transferred into a Teflon-lined stainless steel autoclave (80 mL) for heat treating at 180 °C for 20 h. The precipitate was collected by centrifugation, washed with DI water and ethanol several times, and then dried in a vacuum oven at 80 °C overnight.

2.2. Material characterization

The crystal phases analyses were carried out using a Bruker D8-Avance X-ray diffractometer (XRD) with Cu Kα1 radiation (λ = 0.154056 nm) at 40 kV, 40 mA and a scan rate of 4° min^{-1} in the range of 2θ = 10°–70°. The morphology was observed with Zeiss-Sigma field emission scanning electron microscope (FESEM). High-resolution transmission electron microscopy (HRTEM) was performed at 200 kV on a field-emission electron microscope (JEM2100(HR)) with an ultrahigh-resolution pole piece. UV–vis diffuse reflectance absorption spectroscopy (DRS) spectra were recorded at ambient temperature on a Shimadzu UV-3600 with BaSO$_4$ as the reference sample under scanning scope from 300 to 1000 nm. X-ray photoelectron spectroscopy (XPS) measurement was performed on a Thermo Fisher ESCALAB 250Xi X-ray photoelectron spectroscope equipped with a standard and monochromatic source (Al Kα) operated at 300 W and calibrated with C 1s. Photoluminescence (PL) spectra were carried out on a Hitachi Model F-6800 fluorescence spectrophotometer. Electrochemical data such as transient photocurrent curves were obtained by using a CHI Model 618C electrochemical analyzer and a standard three-electrode system, in which Pt wire, Pt plate, and saturated calomel electrode (SCE) acted as the work, counter, and reference electrode, respectively. In a typical run, the three electrodes were immersed into a suspension containing photocatalyst (10 mg), NaSO$_4$ solution (1.0 M) as electron media, which was continuously purged by N$_2$ flow for 30 min before light irradiation.

2.3. Photocatalytic property tests

The photocatalytic H$_2$ evolution reaction was carried out in a sealed top-irradiation reaction vessel (Pyrex glass). A total of photocatalyst (0.01 g) suspended in aqueous solution (10 mL) containing ascorbic acid (AA) as sacrificial electron donors in the reaction cell. Visible light (λ ≥ 420 nm) was generated by a 300 W Xe-lamp combined with a UV-cutoff filter. Monochromatic light used in the measurement of apparent quantum yield (AQY) was acquired by inserting an appropriate band pass filter ahead of the 300 W Xe-lamp to obtain the correct wavelength, and the light intensity was determined by using a SRC-1000-TC-
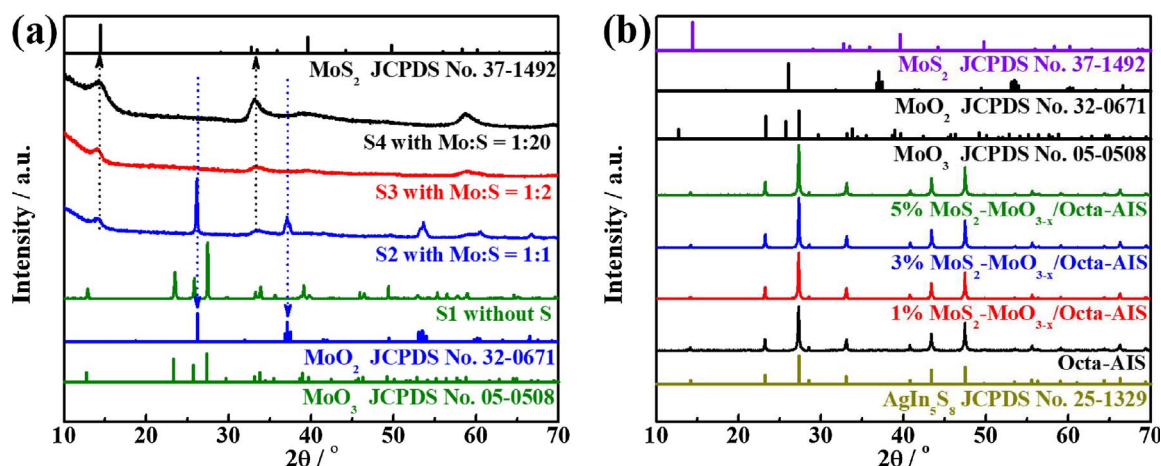
Fig. 1. (a) XRD patterns of the products (S1–S4) derived from the SSR process of $(NH_4)_6Mo_7O_{24}/CS(NH_2)_2$ with different Mo:S molar ratios; (b) XRD patterns of MoS_2-MoO_{3-x}/Octa-AIS with different Mo-loading contents derived from the SSR process of $(NH_4)_6Mo_7O_{24}/CS(NH_2)_2$ with Mo:S mole ratio of 1:1 in the presence of Octa-AIS.

QZ-N monocrystalline silicon cell (Oriel, USA). The AQY values were calculated according to the following equation:

$$AQY(\%) = \frac{\text{number of reacted electrons}}{\text{number of incident photons}} \times 100$$

3. Results and discussion

3.1. Crystal phase and composition analyses of Mo-based cocatalyst

Since the inferior conductivity of multi-layer MoS_2 as co-catalyst will limit the catalytic efficiency [26], simultaneous deposition and growth of MoS_2 and MoO_{3-x} on the pre-prepared $AgIn_5S_8$ nano-octahedrons (Octa-AIS) is conducted through one-step solid-state reaction (SSR) of $(NH_4)_6Mo_7O_{24}/SC(NH_2)_2$ mixture at 380 °C for 3 h under N_2 atmosphere. To make sure the possibility of the formation of MoS_2-MoO_{3-x} cocatalyst, four products (S1–S4) are prepared through the SSR process of $(NH_4)_6Mo_7O_{24}/SC(NH_2)_2$ with different Mo:S molar ratios in the absence of Octa-AIS. As shown in Fig. 1a, product S1 derived from the pyrolysis of $(NH_4)_6Mo_7O_{24}$ without $SC(NH_2)_2$ can be well indexed to an orthorhombic α-MoO_3 (JCPDS No. 05-0508) [30], and there is no other peak ascribable to MoO_2. Nevertheless, the color of product S1 is deep blue but not white as the normal α-MoO_3 (see the insets of Fig. S1a), implying the formation of partially reduced α-MoO_3 (MoO_{3-x}) [33]. To make this issue clear, a fully oxidized MoO_3 (F-MoO_3) was prepared by the pyrolysis of $(NH_4)_6Mo_7O_{24}$ in an air atmosphere, the resultant white powder (see insets of Fig. S1a) has much lower absorption in the range of $\lambda \geq 400$ nm compared to MoO_{3-x} as shown in the diffuse reflectance absorption spectra (DRS, Fig. S1a) even though they have very similar bandgap energy ($E_g = \sim 3.10$ eV) and crystal phase (Fig. S1b). These results imply that the NH_3 gas produced from the pyrolysis of $(NH_4)_6Mo_7O_{24}$ in the N_2 atmosphere can partially reduce α-MoO_3 to form MoO_{3-x} with oxygen-deficient structure and mixed Mo^{5+}/Mo^{6+} oxidation states [33].

With addition of $SC(NH_2)_2$ to Mo:S molar ratio of 1:1, product S2 shows an XRD pattern similar to the monoclinic MoO_2 (JCPDS No. 32-0671) with a portion of Mo being sulfurized into MoS_2 since some weak diffraction peaks can be indexed to hexagonal MoS_2 (JCPDS No. 37-1492) as shown in Fig. 1a [29]. Further enhancing the $SC(NH_2)_2$ content to Mo:S molar ratio of 1:2, product S3 is almost converted into MoS_2, demonstrating the feasibility to synthesize MoS_2 through the present SSR process. Similarly, product S4 derived from the mixture with Mo:S molar ratio up to 1:20 shows an XRD pattern in good agreement with hexagonal MoS_2, and no any peak is ascribable to the other crystals such as MoO_3 or MoO_2. Furthermore, a larger $SC(NH_2)_2$ proportion is beneficial for the growth of MoS_2 since product S4 has

higher crystallinity than product S3 and S2 [34,35].

The above results indicate that the present SSR process can lead to the formation of MoS_2 and/or MoO_{3-x} material, and thus a series of MoS_2-MoO_{3-x}-loaded Octa-AIS (MoS_2-MoO_{3-x}/Octa-AIS) with different Mo-loading contents were synthesized using the SSR process of $(NH_4)_6Mo_7O_{24}/SC(NH_2)_2$ with Mo:S molar ratio of 1:1 in the presence of Octa-AIS. As can be seen from Fig. 1b, all those products show XRD patterns remarkably similar to that of the pristine Octa-AIS, which can be well indexed to the cubic $AgIn_5S_8$ (JCPDS No. 25-1329) [16]. However, there is no any peak ascribable to the crystal phase such as MoO_3, MoO_2, or MoS_2 even for the 5% Mo-loaded product. It might be due to the low loading content and crystallinity of those cocatalyst on the Octa-AIS surface since the survey of X-ray photoelectron spectrum (XPS, Fig. S2) of 5% MoS_2-MoO_{3-x}/Octa-AIS displays obvious Ag 3d, In 3d, S 2p, Mo 3d, and O 1s binding energy peaks.

The chemical composition and valence state of the co-catalysts can be determined from those high resolution XPS spectra (Fig. 2) of 5% MoS_2-MoO_{3-x}/Octa-AIS. The Ag 3d XPS spectrum (Fig. 2a) presents two symmetrical peaks with binding energies at 367.6 (Ag 3d5/2) and 373.7 (Ag 3d3/2) eV, and the In 3d XPS spectrum (Fig. 2b) gives two symmetrical peaks with binding energies at 444.7 (In 3d5/2) and 452.2 (In 3d3/2) eV, indicating the valence states of Ag and In are +1 and +3 [11], respectively. In addition, the S2p spectrum (Fig. 2c) can be deconvoluted into two apparent symmetrical peaks with binding energies at 161.3 (S $2p_{3/2}$) and 162.5 eV (S $2p_{1/2}$), indicating the S exists as -2 oxidation state [34]. The weak O 1s spectrum (Fig. 2d) can be observed from 5% MoS_2-MoO_{3-x}/Octa-AIS, indicating that some Mo-species might exist as oxides, and the deconvoluted main component peak at 531.3 eV corresponds to lattice oxygen (O^{2-}) of MoO_{3-x}, while the weaker component peak at 532.1 eV can be attributed to surface adsorbed species such as OH^- [30].

The Mo 3d spectrum (Fig. 3a) of 5% MoS_2-MoO_{3-x}/Octa-AIS can be divided into six peaks, the binding energy peaks at 232.8 and 236.0 eV can be ascribed to Mo^{6+} $3d_{5/2}$ and Mo^{6+} $3d_{3/2}$ of MoO_3 [34], while the peak at 232.3 and 235.4 eV corresponds to Mo^{5+} $3d_{5/2}$ and Mo^{5+} $3d_{3/2}$, indicating the existence of Mo^{5+} in MoO_3 which owing to the partial reduction of MoO_3 to form MoO_{3-x} with oxygen-deficient structure [34]. Moreover, the other two peaks of Mo 3d at around 229.3 and 232.5 eV are the characteristics of +4 oxidation state, indicating the coexistence of MoS_2 with MoO_{3-x} [30]. To make this issue clear, two contrast samples (MoO_{3-x}/Octa-AIS and MoS_2/Octa-AIS) were prepared and used to determine the Mo 3d XPS spectra. As can be seen from Fig. 3b, MoO_{3-x}/Octa-AIS derived from the pyrolysis of $(NH_4)_6Mo_7O_{24}$ without $SC(NH_2)_2$ in the presence of Octa-AIS exhibits +5 and +6 oxidation states with the binding energy peaks of Mo^{5+} at 232.3 (Mo^{5+} $3d_{5/2}$)/235.4 (Mo^{5+} $3d_{3/2}$) eV and Mo^{6+} at 232.9 (Mo^{6+} $3d_{5/2}$)/
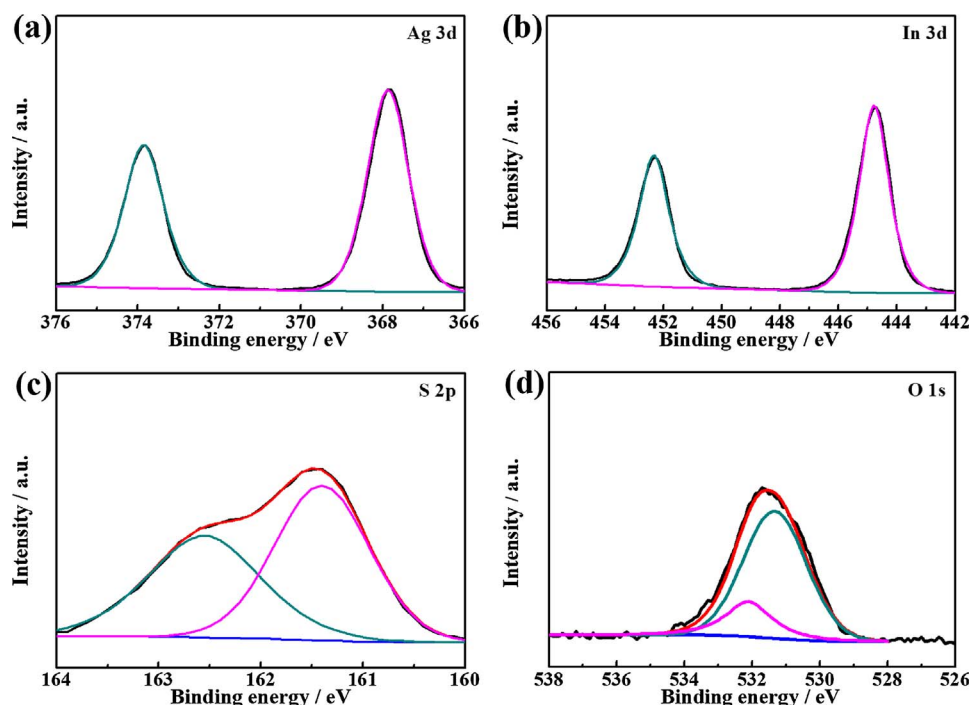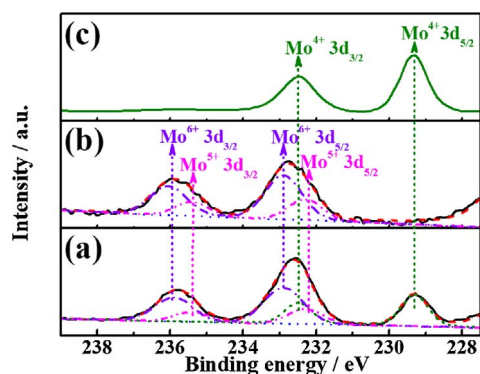
Fig. 3. The high resolution Mo 3d XPS spectra of 5% MoS_2-MoO_{3-x}/Octa-AIS (a) and two contrast samples (MoO_{3-x}/Octa-AIS (b) and MoS_2/Octa-AIS (c)).

236.1 eV (Mo^{6+} $3d_{3/2}$) eV, which are similar to that of MoS_2-MoO_{3-x}/Octa-AIS shown in Fig. 3a. This result demonstrates that the pyrolysis process of $(NH_4)_6Mo_7O_{24}$ in N_2 atmosphere can form partially reduced MoO_{3-x} even in the presence of Octa-AIS. However, MoS_2/Octa-AIS derived from the SSR process of $(NH_4)_6Mo_7O_{24}$/$SC(NH_2)_2$ with Mo:S molar ratio of 1:20 in the presence of Octa-AIS only shows the signals of +4 oxidation state (Fig. 3c) with binding energy peaks at 229.3 (Mo^{4+} $3d_{5/2}$) and 232.5 (Mo^{4+} $3d_{5/2}$) eV, consistent with literature values of MoS_2 [30], indicating that enhancing the $SC(NH_2)_2$ proportion in the $(NH_4)_6Mo_7O_{24}$/$SC(NH_2)_2$ mixture is beneficial for the growth of MoS_2 on Octa-AIS surface.

The above results demonstrate that the present SSR process of $(NH_4)_6Mo_7O_{24}$/$SC(NH_2)_2$ with Mo:S molar ratio of 1:1 results in the formation of MoS_2-MoO_{3-x} hybrid cocatalyst on Octa-AIS surface, and the surface atomic molar ratio of Mo^{6+}/Mo^{5+}/Mo^{4+} in 5% MoS_2-MoO_{3-x}/Octa-AIS can be calculated to be 49/18/33 according to the XPS spectra shown in Fig. 3a. Further evidence for this issue can be found from Fig. S3. The 5% MoS_2-MoO_{3-x}/Octa-AIS contains many uniform nano-octahedron-like particles (Fig. S3a), which is very similar to the that of $AgIn_5S_8$ nano-octahedrons with an average size of ~ 260 nm as our previous report [16]. It indicates that the morphology of the pre-prepared Octa-AIS was not influenced by the present SSR

process for loading the Mo-based cocatalyst. Also, the XRD patterns (Fig. 1b) show no obvious influence on the crystal phase and crystallinity. Nevertheless, many finite irregular nanoparticles exist around those nano-octahedrons (Fig. S3a), and some of those nanoparticles locate on the exposed (111) facets of nano-octahedrons as shown in the TEM image (Fig. S3b). Also, the TEM image at higher magnification (Fig. 4a) indicates many small nanoparticles located on the nano-octahedron's facets, and the HRTEM image (Fig. 4b) shows that those nanoparticles contain two morphologies. Namely, in addition to nanoparticles with interlayer spacings of ca. 0.326 nm, which corresponds to the (021) planes of orthorhombic MoO_{3-x} [27], few-layer nanosheets with interlayer spacings of ca. 0.620 nm, which corresponds to the (002) planes of hexagonal MoS_2 [28], are loaded on the nano-octahedron surface. This is consistent with the above Mo 3d XPS spectra, in which there is coexistence of Mo^{6+}, Mo^{5+} and Mo^{4+} species. The contrast sample MoO_{3-x}/Octa-AIS exhibits no any nanosheet-like particle loaded on the Octa-AIS (Fig. 4c), and those nanoparticles on the Octa-AIS surface has interlayer spacings of ca. 0.326 nm (Fig. 4d), corresponding to the (021) planes of MoO_{3-x} [27]. As for the contrast sample MoS_2/Octa-AIS, there are mainly nanosheet-like particles loaded on Octa-AIS surface (Fig. 4e), and the corresponding interlayer spacings of ca. 0.620 nm correspond well with the (002) planes of MoS_2 (Fig. 4f) [28], which is consistent with the finding that the Mo 3d XPS spectrum (Fig. 3c) of MoS_2/Octa-AIS only contains Mo^{4+} species. It indicates that the existence of $SC(NH_2)_2$ in the present SSR process can lead to the formation of nanosheet-like MoS_2 on Octa-AIS surface. The above results demonstrate that MoS_2-MoO_{3-x} hybrid cocatalyst can be successfully deposited on the Octa-AIS surface and their close contacts is believed to favor the directional transfer of the photogenerated electrons from Octa-AIS to MoO_{3-x} nanoparticles and/or few-layer MoS_2 nanosheets, and thus to improve the charge separation and photocatalytic efficiency.

3.2. Formation mechanism and spectral absorption analyses of Mo-based cocatalyst

Based on the above results and discussion, it can be concluded that MoS_2-MoO_{3-x} hybrid cocatalyst can be successfully deposited on Octa-AIS surface through the present SSR process of $(NH_4)_6Mo_7O_{24}$/
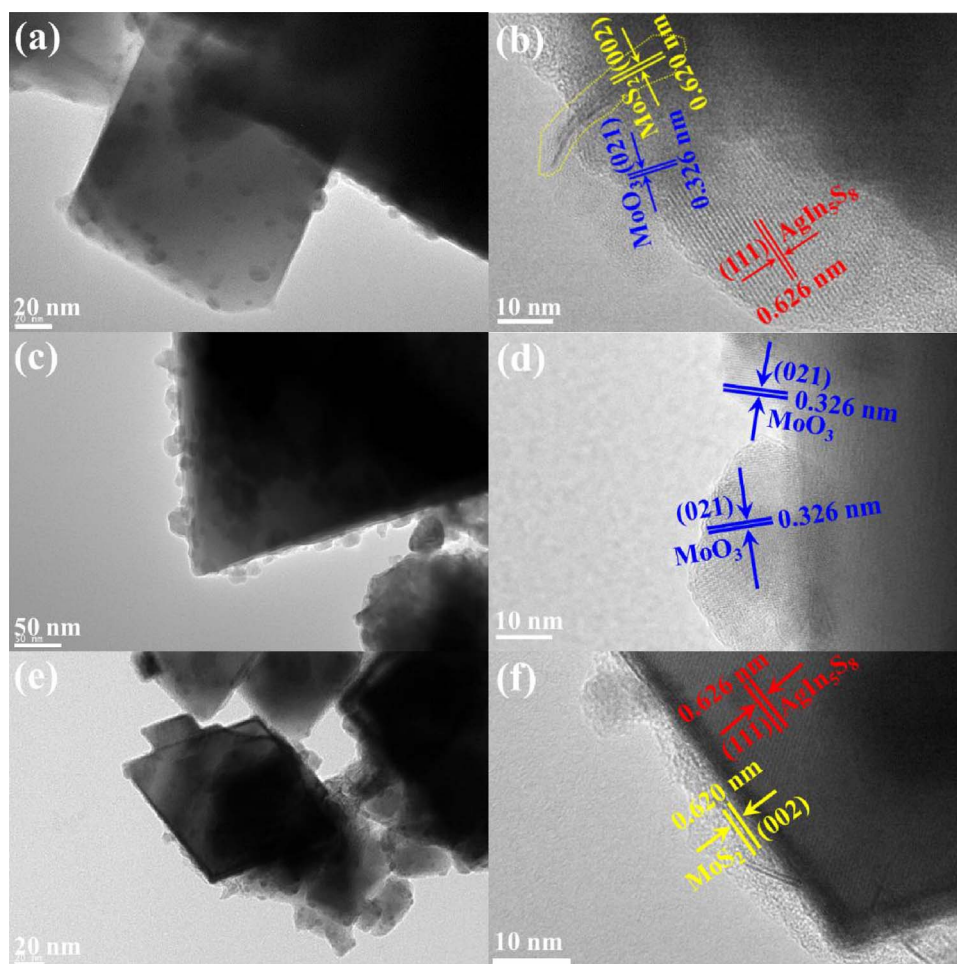
Fig. 4. TEM and HRTEM images of 5% MoS$_2$-MoO$_{3-x}$/Octa-AIS (a, b) and two contrast samples (MoO$_{3-x}$/Octa-AIS (c, d) and MoS$_2$/Octa-AIS (e, f)).
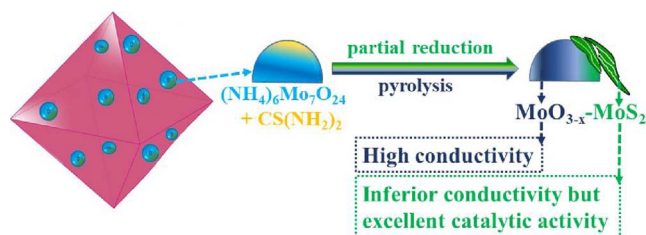

Fig. 5. The possible formation mechanism of the binary Mo-based cocatalyst (MoS$_2$-MoO$_{3-x}$) on Octa-AIS during the SSR process.

SC(NH$_2$)$_2$ with Mo:S molar ratio of 1:1, the corresponding growth process can be illustrated diagrammatically in Fig. 5. As mentioned above, the pyrolysis of (NH$_4$)$_6$Mo$_7$O$_{24}$ without SC(NH$_2$)$_2$ leads to the formation of MoO$_{3-x}$ nanoparticles due to the reductive NH$_3$ gas produced from the pyrolysis of (NH$_4$)$_6$Mo$_7$O$_{24}$ in the N$_2$ atmosphere [33]. Those MoO$_{3-x}$ nanoparticles with oxygen-deficient structure and mixed Mo^{5+}/Mo^{6+} oxidation states have relatively high conductivity, and thus favor the photogenerated electron transport and then the H$_2$ evolution [30]. When sufficient S source is supplied during the SSR process, the Mo^{6+} species in (NH$_4$)$_6$Mo$_7$O$_{24}$ can be reduced to form few-layer MoS$_2$ nanosheets, which is also a benefit to the enhancement of the photoactivity since the inferior conductivity of multi-layer and larger MoS$_2$ as co-catalyst would limit the enhancement of the photocatalytic efficiency [36]. Hence, it can be concluded that the present SSR process can partially reduce the decomposition product of the (NH$_4$)$_6$Mo$_7$O$_{24}$/SC(NH$_2$)$_2$ mixture to form MoO$_{3-x}$ and MoS$_2$ on the Octa-AIS surface as shown in Fig. 5, and the proportion of MoS$_2$ can be

controlled by adjusting the SC(NH$_2$)$_2$ addition amount. Moreover, the present SSR process is also an effective way to stabilize the binding of the Mo-based cocatalyst with the Octa-AIS surface and to realize the close contacts of Octa-AIS, MoS$_2$ and MoO$_{3-x}$ components, which will favor the synergetic effects of the MoO$_{3-x}$ nanoparticles with high conductivity and the few-layer MoS$_2$ nanosheets with excellent catalytic property, and then causing an enhanced charge separation and photocatalytic efficiency for H$_2$ evolution.

The DRS spectra (Fig. 6) show that the pristine Octa-AIS has an absorption band edge at around 736 nm, corresponding to its bandgap energy of about 1.68 eV, which is similar to the previous reported values [14–16]. Nevertheless, those MoS$_2$-MoO$_{3-x}$/Octa-AIS nanocomposites exhibit red-shifts in the absorption band edges and elevated
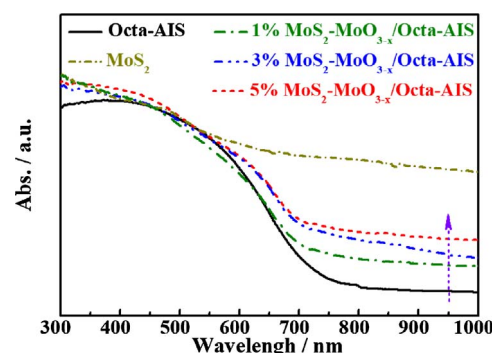

Fig. 6. Diffuse reflectance absorption spectra (DRS) of Octa-AIS with different MoS$_2$-MoO$_{3-x}$ loading contents.

backgrounds in the range of 700–1000 nm, which show an increasing trend along with enhancing the MoS_2-MoO_{3-x} contents. For instance, the absorption band edges of the 1%, 3% and 5% MoS_2-MoO_{3-x}/Octa-AIS products locate at around 762, 783 and 792 nm, corresponding to a bandgap energy of about 1.63, 1.59 and 1.57 eV, respectively. On the one hand, the elevated backgrounds could be attributed to the enhancement of MoS_2 content in those nanocomposites since MoS_2 has significant spectral responses in the range of visible and near infrared light regions as shown in Fig. 6 [22–24]. Similarly, an enhanced MoO_{3-x} content also contributes to the enhancement in the background absorptions as shown in Fig. S1a. On the other hand, the formation of MoS_2-MoO_{3-x} hybrids with $Mo^{6+}/Mo^{5+}/Mo^{4+}$ oxidation states and the possible change of the Octa-AIS surface due to the reducing atmosphere during the present SSR process would lead to the absorption band-edge red-shifts of those MoS_2-MoO_{3-x}/Octa-AIS products. Therefore, it can be inferred that the introduction of MoS_2-MoO_{3-x} on the Octa-AIS surface would have influence on the fundamental process of the spectral absorption, photogenerated carrier formation and separation during the photocatalytic process, which will be further discussed below.

3.3. Effects of Mo-based cocatalyst on the photocatalytic activity and mechanism of octa-AIS

The photocatalytic performance of Octa-AIS loaded with various cocatalysts were studied, and the primary experiments indicate that photocatalyst (10 mg) suspended in ascorbic acid (AA) aqueous solution (10 mL, 50 mM) under visible light ($\lambda \geq 420$ nm) irradiation is an optimal photoreaction condition. As can be seen from Fig. 7, MoO_{3-x}/Octa-AIS acquires a H_2 evolution activity of 28 μmol h^{-1}, which is 4.3 times of that (6.5 μmol h^{-1}) of the pristine Octa-AIS, indicating that MoO_{3-x} can also act as co-catalyst to promote the H_2 evolution reaction over the Octa-AIS. As mentioned above, a certain amount of MoS_2 can be produced along with the formation of those MoO_{3-x} nanoparticles on the Octa-AIS surfaces in the presence of $CS(NH_2)_2$ (Mo: S molar ratio of 1: 1), and the formed few-layer MoS_2 nanosheets tend to contact with MoO_{3-x} nanoparticles on the (111) facets of Octa-AIS as observed from the TEM image (Fig. 4b). The corresponding MoS_2-MoO_{3-x}/Octa-AIS achieves a much higher H_2 evolution activity (117 μmol h^{-1}) than MoO_{3-x}/Octa-AIS and Octa-AIS, demonstrating that those few-layer MoS_2 nanosheets can act as co-catalyst to further promote the catalytic reaction for H_2 evolution over the Octa-AIS. Nevertheless, the Mo^{6+} species in $(NH_4)_6Mo_7O_{24}$ are completely reduced to MoS_2 when the Mo:S molar ratio of $(NH_4)_6Mo_7O_{24}/SC(NH_2)_2$ is enhanced to 1:20, and the resultant MoS_2/Octa-AIS shows a lower H_2 evolution activity (86 μmol h^{-1}) than MoS_2-MoO_{3-x}/Octa-AIS (117 μmol h^{-1}) even though it is much better than that (28 μmol h^{-1}) of MoO_{3-x}/Octa-AIS. The above results indicate that the present MoS_2-MoO_{3-x} cocatalyst has

certain synergetic effect on the enhancement of H_2 evolution activity over the Octa-AIS.

To further expound the reason for the enhanced activity after loading with MoS_2-MoO_{3-x} cocatalyst on the Octa-AIS surface, 3% MoS_2-loaded $AgIn_5S_8$ (MoS_2/AIS) was synthesized through one-pot hydrothermal process. It was found that the H_2 evolution activity (6.8 μmol h^{-1}, Fig. 7) is similar to that (6.5 μmol h^{-1}) of the pristine Octa-AIS but much lower than that (86 μmol h^{-1}) of MoS_2/Octa-AIS. This can be explained by the differences in their microstructures. As shown in Fig. S4, those resultant MoS_2/AIS shows obvious two-phase separation between $AgIn_5S_8$ and MoS_2, and those MoS_2 grow into large hierarchical structures, which leads to the photogenerated electrons of AIS could not effectively transfer to MoS_2 smoothly. Moreover, those MoS_2 agglomerates have smaller specific surface area and less active edge centers [26,36], and thus causing the much lower photoactivity. This result indicates that the one-pot hydrothermal process for the preparation of MoS_2/AIS is not appropriate to effectively deposit the MoS_2 cocatalyst on the AIS surface. Whereas the present Octa-AIS with high crystallinity and less defects in the exposed (111) facets are beneficial for the formation of few-layer MoS_2 nanosheets to closely contact with the Octa-AIS surface as shown in the TEM image (Fig. 4f). The (002) planes of those few-layer MoS_2 nanosheets with 2D layered structure can well contact with the exposed (111) facets of Octa-AIS as shown in Fig. S5, which can promote the charge separation and provide more undercoordinated S-atoms at the edges of MoS_2 as active centers for the H_2 evolution reaction [4,26,34].

The photoactivities of Octa-AIS with various MoS_2-MoO_{3-x} loading contents are measured and shown in Fig. 8a. As can be seen, the H_2 evolution activity shows an increasing trend along with enhancing the MoS_2-MoO_{3-x} content from 0 to 3%, and then a decreasing one with further increasing the loading content. The 3% MoS_2-MoO_{3-x}/Octa-AIS product achieves the highest H_2 evolution activity (117 μmol h^{-1}), demonstrating that MoS_2-MoO_{3-x} as co-catalyst has an optimal loading content. Possibly, the increasing H_2 evolution activity stems from the much more active sites provided by more cocatalyst, while excessive MoS_2-MoO_{3-x} loading on the exposed (111) facets would inhibit the reactant adsorption for the H_2 evolution reaction [18]. Similarly, the precious metal Pt as cocatalyst on Octa-AIS also exhibits a similar changing trend along with enhancing the loading content as shown in Fig. 8b, whereby 1.0% Pt/Octa-AIS achieves a maximum H_2 evolution activity (49.0 μmol h^{-1}). Obviously, MoS_2-MoO_{3-x} as cocatalyst with an optimal loading content acquires much better H_2 evolution activity than Pt under the present photoreaction condition.

The better photoactivity of MoS_2-MoO_{3-x}/Octa-AIS than Pt/Octa-AIS can be validated by the photoluminescence (PL) spectra (Fig. 9a), in which the pristine Octa-AIS shows an intensive fluorescence intensity due to serious recombination of photogenerated carriers after photo-excitation, which can be effectively quenched by loading MoS_2-MoO_{3-x} or Pt due to the capture of the photogenerated electrons of Octa-AIS. The more significant fluorescence quenching of MoS_2-MoO_{3-x} than Pt on Octa-AIS implies the more effective charge transfer [11,37]. This conjecture can be confirmed by the experimental result that MoS_2-MoO_{3-x}/Octa-AIS possesses greater transient photocurrent response than Pt/Octa-AIS as shown in Fig. 9b. It indicates that MoS_2/MoO_{3-x} as cocatalyst acquires better interfacial charge transfer performance, which can retard the photogenerated charge recombination, then cause the better photoactivity than Pt/Octa-AIS.

Fig. 10 depicts the wavelength-dependent apparent quantum yield (AQY) values of MoS_2-MoO_{3-x}/Octa-AIS and Pt/Octa-AIS under various monochromatic light irradiation with band-pass filters (λ = 435, 450, 475, 500, 520, 570, 600, 660, 685, 700, 720 ± 10 nm). As can be seen, the variation tendencies of AQY curves at the long wavelength regions for both MoS_2-MoO_{3-x}/Octa-AIS and Pt/Octa-AIS are similar to the DRS spectrum of Octa-AIS, and there is no obvious H_2 evolution when the monochromatic light wavelength is ≥720 nm. Namely, the wavelengths suitable for H_2 evolution are found to coincide with the

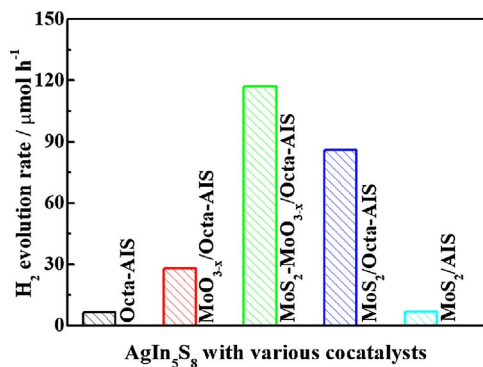**Fig. 7.** Photocatalytic H_2 evolution activity of Octa-AIS and its 3% MoO_{3-x}, MoS_2-MoO_{3-x}, MoS_2 loaded products under visible light ($\lambda \geq 420$ nm) irradiation. Conditions: 10 mg photocatalysts in 10 mL AA aqueous solution (50 mM). 3% MoS_2/AIS is prepared through a one-pot hydrothermal process at 180 °C for 24 h.
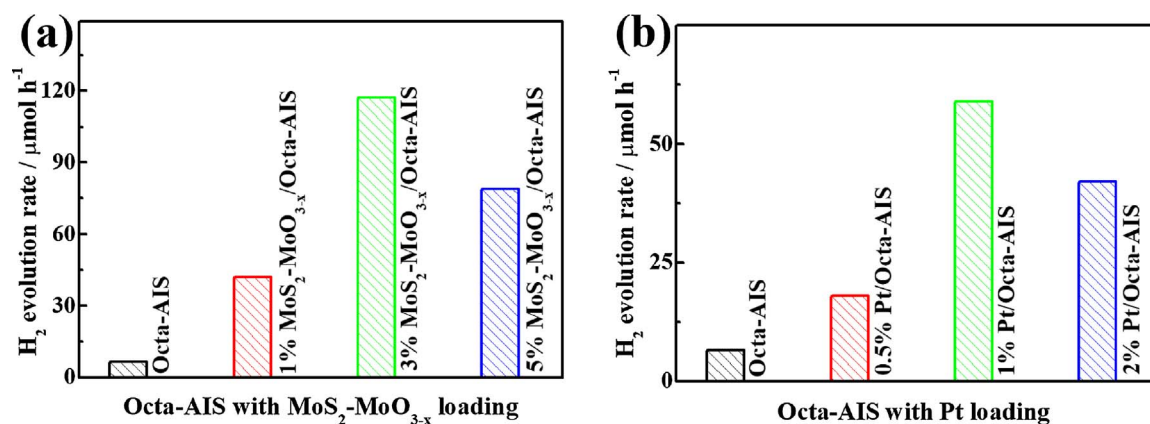
Fig. 8. Photocatalytic H_2 evolution activity of Octa-AIS with different loading contents of MoS_2-MoO_{3-x} (a) and Pt (b) under visible light ($\lambda \geq 420$ nm) irradiation. Conditions: 10 mg photocatalysts in 10 mL of AA aqueous solution (50 mM).
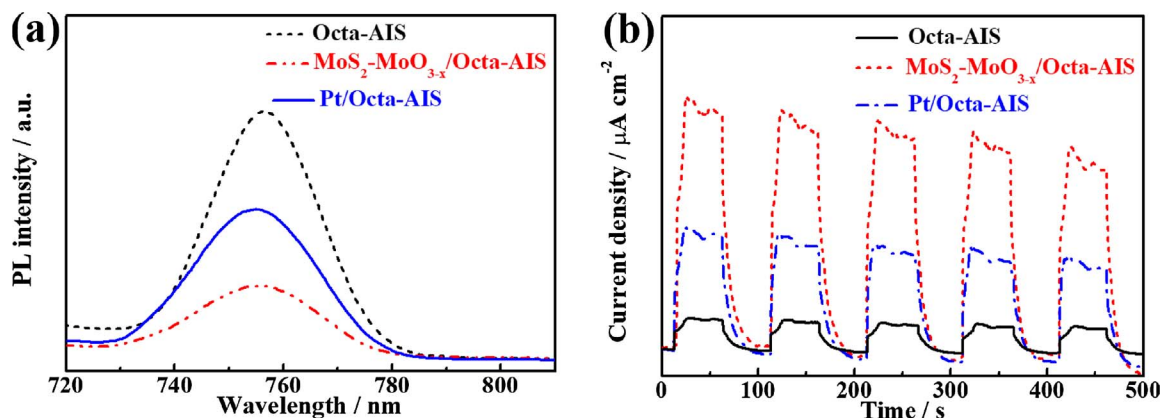

Fig. 9. Photoluminescence (PL) spectra (a) and transient photocurrent responses (b) of Octa-AIS, 3% MoS_2-MoO_{3-x}/Octa-AIS, and 1% Pt/Octa-AIS.
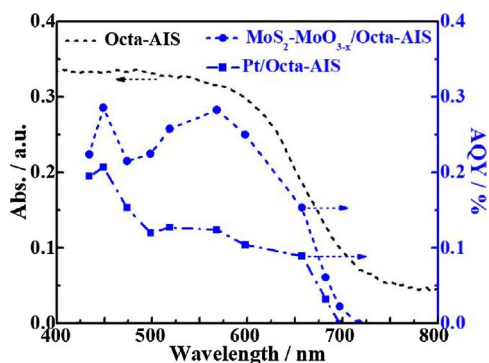

Fig. 10. Wavelength-dependent AQY values of 3% MoS_2-MoO_{3-x}/Octa-AIS and 1% Pt/Octa-AIS and the DRS spectrum of Octa-AIS.

Fig. 11. Time courses of H_2 evolution over 3% MoS_2-MoO_{3-x}/Octa-AIS or 1% Pt/Octa-AIS suspension system under visible light ($\lambda \geq 420$ nm) irradiation. Conditions: 10 mg photocatalysts in 10 mL AA solution (50 mM).

absorption edge of the pristine Octa-AIS even though those photocatalysts still show high background adsorption in the range of $\lambda \geq 720$ nm (Fig. 6). It indicates that the H_2 evolution reaction was indeed driven by the photoexcitation process of Octa-AIS, and its light absorption property governs the photoactivity for H_2 evolution, while those loaded MoS_2-MoO_{3-x} and Pt serving as cocatalyst but not light absorber. Once again, MoS_2-MoO_{3-x} as co-catalyst acquires a relatively higher AQY values within the entire measured wavelength region compared to Pt, indicating that the present Mo-based binary cocatalyst displays faster charge transfer rate and better catalytic property during the photocatalytic reaction processes.

The time courses (Fig. 11) of H_2 evolution exhibit both MoS_2-MoO_{3-x}/Octa-AIS and Pt/Octa-AIS have relatively good long-term stability in the three consecutive runs, in which fresh sacrificial reagent solution is
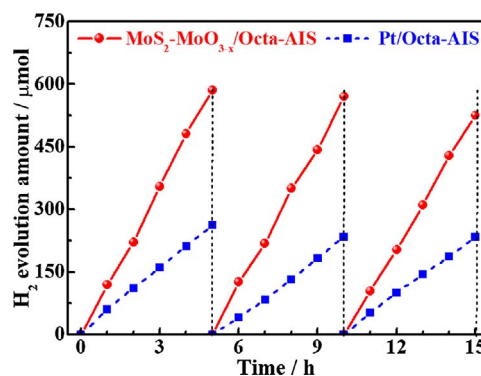
replaced periodically in each run. As can be seen, 3% MoS_2-MoO_{3-x}/Octa-AIS exhibits an average H_2 evolution rate of 117 μmol h^{-1} in the first run of 5 h photoreaction and then slightly declines to 114 and 105 μmol h^{-1} in the second and third run of 5 h photoreaction, respectively. The percentages of the H_2-evolution rate of the second and third run as compared to the first run's are calculated to be 97.4% and 90.0%, respectively. This decrease in photocatalytic performance may be due to the relatively poor stability of Octa-AIS since it a typical sulfide photocatalyst. In addition, the oxidation of the edge active sites of MoS_2 nanosheets and the instability of MoO_{3-x} nanoparticles are also responsible for the inactivation [38]. Nevertheless, 1% Pt/Octa-AIS shows more obvious declines in the H_2 evolution rate in the three
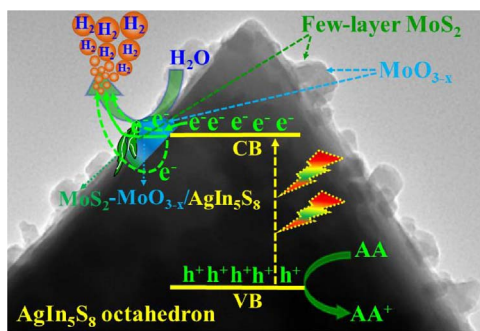
Fig. 12. The probable mechanism for H_2 evolution over the MoS_2-MoO_{3-x}/AIS.

consecutive runs with an average H_2 evolution rate of 52.4, 46.8, and 43.4 µmol h^{-1} in the first, second, and third run of 5 h photoreaction, respectively. After the third run, the corresponding percentages of the H_2 evolution rate as compared to the first run's is calculated to be 82.8%. The above results indicate that MoS_2-MoO_{3-x} as cocatalyst on Octa-AIS has better stability for H_2 evolution than Pt in the present photoreaction system.

Although it was found that MoO_{3-x} like MoS_2 can also act as cocatalyst to promote the catalytic reaction for the visible-light-driven H_2 evolution over Octa-AIS, the simultaneous deposition of the binary cocatalyst can effectively enhance the H_2 evolution activity over Octa-AIS as shown in Fig. 7. The oxygen-deficient MoO_{3-x} nanoparticles retain the layered orthorhombic structure of the parent material, and thus enable facile charge transport due to its high conductivity [33,34], while the few-layer MoS_2 nanosheets provide more edge active sites for more effective catalytic reaction [26,30]. The close neighborhood among the Octa-AIS, MoS_2 and MoO_{3-x} components in MoS_2-MoO_{3-x}/Octa-AIS is a benefit to exerting the synergetic effects of the MoO_{3-x} nanoparticles with high conductivity and the few-layer MoS_2 nanosheets with excellent catalytic property, which favor the directional transfer of photogenerated electrons from Octa-AIS to MoO_{3-x} nanoparticles and/or the few-layer MoS_2 nanosheets as shown in Fig. 12, and then causing the enhanced charge separation and photocatalytic efficiency for H_2 evolution. The above results demonstrate the feasibility of the present binary Mo-based cocatalysts replacing the precious metal Pt, which is of great significance in developing the practical H_2 evolution system with better activity and stability.

4. Conclusion

A new binary Mo-based cocatalyst consisting of partially reduced α-MoO_3 (MoO_{3-x}) nanoparticles and few-layer MoS_2 nanosheets is deposited on $AgIn_5S_8$ nano-octahedrons (Octa-AIS) with only (111) facets exposed *via* an *in situ* growth process. Although it was found that the single MoO_{3-x} or MoS_2 as cocatalyst can promote the catalytic reaction for the visible-light-driven H_2 evolution on Octa-AIS, the simultaneous deposition of MoS_2-MoO_{3-x} hybrid cocatalyst shows more effective enhancement of the H_2 evolution activity over Octa-AIS. The close neighborhood among the Octa-AIS, MoS_2 and MoO_{3-x} components in MoS_2-MoO_{3-x}/Octa-AIS is a benefit to exerting the synergetic effects of the MoO_{3-x} nanoparticles with high conductivity and the few-layer MoS_2 nanosheets with excellent catalytic property, which favor the photogenerated electrons transferring from Octa-AIS to MoO_{3-x} nanoparticles and/or the few-layer MoS_2 nanosheets, and thus causing the enhanced charge separation and photocatalytic efficiency for H_2 evolution. The above microstructured feature results in the MoS_2-MoO_{3-x} as cocatalyst on Octa-AIS showing better photoactivity and stability for H_2 evolution than Pt nanoparticles. This study not only presents the first example of binary Mo-based cocatalyst with synergetic effect between MoS_2 and MoO_{3-x} components, but also paves a new way to develop an inexpensive photocatalytic system for solar energy conversion to

achieve highly efficient H_2 evolution without noble metal-loading.

Appendix A. Supplementary data

Supplementary material related to this article can be found, in the online version, at doi:https://doi.org/10.1016/j.apcatb.2018.01.077.

References

[1] A. Fujishima, K. Honda, Nature 238 (1972) 37–38.
[2] A. Kudo, Y. Miseki, Chem. Soc. Rev. 38 (2009) 253–278.
[3] X.H. Zhang, T.Y. Peng, S.S. Song, J. Mater. Chem. A 4 (2016) 2365–2402.
[4] X. Zong, H.J. Yan, D.P. Wu, G.J. Ma, F.Y. Wen, L. Wang, C. Li, J. Am. Chem. Soc. 130 (2008) 7176–7177.
[5] J.M. Wang, Y. Zhen, T.Y. Peng, J. Zhang, R.J. Li, ACS Sustain. Chem. Eng. 5 (2017) 7549–7556.
[6] X.H. Zhang, B.S. Peng, T.Y. Peng, L.J. Yu, R.J. Li, J. Zhang, J. Power Sources 298 (2015) 30–37.
[7] X.H. Zhang, T.Y. Peng, L.J. Yu, R.J. Li, Q.Q. Li, Z. Li, ACS Catal. 5 (2015) 504–510.
[8] X.H. Zhang, L.J. Yu, C.S. Zhuang, T.Y. Peng, R.J. Li, X.G. Li, ACS Catal. 4 (2014) 162–170.
[9] I. Tsuji, H. Kato, A. Kudo, Angew. Chem. Int. Ed. 44 (2005) 3565–3568.
[10] C.H. Lai, C.Y. Chiang, P.C. Lin, K.Y. Yang, C.C. Hua, T.C. Lee, ACS Appl. Mater. Interfaces 5 (2013) 3530–3540.
[11] K. Li, B. Chai, T.Y. Peng, J. Mao, L. Zan, ACS Catal. 3 (2013) 170–177.
[12] K. Li, J.L. Xu, X.H. Zhang, T.Y. Peng, X.G. Li, Int. J. Hydrogen Energy 38 (2013) 15965–15975.
[13] K.W. Cheng, C.M. Huang, G.T. Pan, W.S. Chang, T.C. Lee, T.C.K. Yang, J. Photochem. Photobiol. A 190 (2007) 77–87.
[14] X.Q. Li, L. Wang, D.L. Wei, S.Z. Kang, J. Mu, Mater. Res. Bull. 48 (2013) 286–289.
[15] W.J. Zhang, D.Z. Li, M. Sun, Y. Shao, Z.X. Chen, G.C. Xiao, X.Z. Fu, J. Solid State Chem. 183 (2010) 2466–2474.
[16] S.S. Song, Z.C. Liang, W.L. Fu, T.Y. Peng, ACS Appl. Mater. Interfaces 9 (2017) 17013–17023.
[17] J. Yang, D. Wang, H. Hanm, C. Li, Acc. Chem. Res. 46 (2013) 1900–1909.
[18] J.R. Ran, J. Zhang, J.G. Yu, M. Jaroniec, S.Z. Qiao, Chem. Soc. Rev. 43 (2014) 7787–7812.
[19] S. Trasatti, J. Electroanal. Chem. Interfacial Electrochem. 39 (1972) 163–184.
[20] T.F. Jaramillo, K.P. Jørgensen, J. Bonde, J.H. Nielsen, S. Horch, I. Chorkendorff, Science 317 (2007) 100–102.
[21] B. Radisavljevic, A. Radenovic, J. Brivio, V. Giacometti, A. Kis, Nat. Nanotechnol. 6 (2011) 147–150.
[22] Y.H. Lee, L. Yu, H. Wang, W. Fang, X. Ling, Y. Shim, C.T. Lin, J.K. Huang, M.T. Chang, C.S. Chang, M. Dresselhaus, T. Palacios, L.J. Li, J. Kong, Nano Lett. 13 (2013) 1852–1857.
[23] R. Lv, J.A. Robinson, R.E. Schaak, D. Sun, Y. Sun, T.E. Mallouk, M. Terrones, Acc. Chem. Res. 48 (2015) 56–64.
[24] M. Chhowalla, H.S. Shin, G. Eda, L.J. Li, K.P. Loh, H. Zhang, Nat. Chem. 5 (2013) 263–275.
[25] D. Voiry, A. Goswami, R. Kappera, C.C. Silva, D. Kaplan, T. Fujita, M. Chen, T. Asefa, M. Chhowalla, Nat. Chem. 7 (2015) 45–49.
[26] B. Hinnemann, P.G. Moses, J. Bonde, K.P. Jørgensen, J.H. Nielsen, S. Horch, I. Chorkendorff, J.K. Nørskov, J. Am. Chem. Soc. 127 (2005) 5308–5309.
[27] Y. Hou, A.B. Laursen, J. Zhang, G. Zhang, Y. Zhu, X. Wang, S. Dahl, Angew. Chem. Int. Ed. 52 (2013) 3621–3625.
[28] Q.J. Xiang, J.G. Yu, M. Jaroniec, J. Am. Chem. Soc. 134 (2012) 6575–6578.
[29] W. Zhou, Z. Yin, Y. Du, X. Huang, Z. Zeng, Z. Fan, H. Liu, J. Wang, H. Zhang, Small 9 (2013) 140–147.
[30] R. Luo, R. Miao, T.D. Huan, I.M. Mosa, A.S. Poyraz, W. Zhong, J.E. Cloud, D.A. Kriz, S. Thanneeru, J. He, Y. Zhang, R. Ramprasad, S.L. Suib, Adv. Energy Mater. 6 (2016) 1600528–1600539.
[31] R. Wu, J. Zhang, Y. Shi, D. Liu, B. Zhang, J. Am. Chem. Soc. 137 (2015) 6983–6986.
[32] C.J. Machiels, W.H. Cheng, U. Chowdhry, W.E. Farneth, F. Hong, E.M. Mc Carron, A.W. Sleight, Appl. Catal. 25 (1986) 249–256.
[33] H.S. Kim, J.B. Cook, H. Lin, J.S. Ko, S.H. Tolbert, V. Ozolins, B. Dunn, Nat. Mater. 16 (2017) 454–460.
[34] X. Chen, D. Cummins, B.N. Reinecke, E. Clark, M.K. Sunkara, T.F. Jaramillo, Nano Lett. 11 (2011) 4168–4175.
[35] J. Li, G. Zhan, Y. Yu, L. Zhang, Nat. Commun. 7 (2016) 11480.
[36] F. Wang, G. Dukovic, L.E. Brus, T.F. Heinz, Phys. Rev. Lett. 92 (2004) 177401.
[37] H. Li, J. Shang, Z.H. Ai, L.Z. Zhang, J. Am. Chem. Soc. 137 (2015) 6393–6399.
[38] E. Parzinger, B. Miller, B. Blaschke, J.A. Garrido, J.W. Ager, A. Holleitner, U. Wurstbauer, ACS Nano 9 (2015) 11302–11309.